Construction of urchin-like $ZnIn_2S_4$-Au-TiO_2 heterostructure with enhanced activity for photocatalytic hydrogen evolution

Guang Yang[a], Hao Ding[a,*], Daimei Chen[a,*], Jiejie Feng[a], Qiang Hao[a], Yongfa Zhu[b]

[a] Beijing Key Laboratory of Materials Utilization of Nonmetallic Minerals and Solid Wastes, National Laboratory of Mineral Materials, School of Materials Science and Technology, China University of Geosciences, Xueyuan Road, Haidian District, Beijing, 100083, China
[b] Department of Chemistry, Tsinghua University Beijing, 100084, China

ABSTRACT

The ternary $ZnIn_2S_4$-Au-TiO_2 Z-scheme heterostructure photocatalysts has been fabricated by selecting effectiveness Au NPs as a solid electron mediator, via a chemical-deposition process for water splitting under simulated solar light irradiation. The designed photocatalysts exhibit high surface area and wide light absorption range, which significantly enhance photocatalytic efficiency. At an optimal ratio of 24 wt% Au NPs and 60 wt% $ZnIn_2S_4$, the obtained $ZnIn_2S_4$-Au-TiO_2 photocatalysts achieve the highest H_2 production with the rate of 186.3 $\mu mol\, g^{-1}\, h^{-1}$, and the O_2 production rate is reached to 66.3 $\mu mol\, g^{-1}\, h^{-1}$. It showed that the $ZnIn_2S_4$-Au-TiO_2 composite structures exhibit significantly better photocatalytic activity than $ZnIn_2S_4$-TiO_2 and Au-$ZnIn_2S_4$-TiO_2 structure. Such an excellent performance should be attributed to the Au NPs in the Z-scheme system structure which favor to enhance the transfer rate of the photogenerated electrons and holes and remain strong redox ability of the photocatalysts. It is worth pointing out that the unique Z-scheme $ZnIn_2S_4$-Au-TiO_2 heterostructure shows great solar activity toward water splitting into renewable hydrocarbon fuel.

1. Instruction

Solar water splitting utilizing photocatalysts have attracted a tremendous amount of interest over the past decades becauses it presents highly promising alternative to provide clean hydrogen energy by using of sunlight [1–3]. It is widely known that TiO_2 is one of the most effective photocatalysts in the field of environmental cleaning and hydrogen energy production due to its several major factors such as abundant morphologies, easy synthesis, chemical stability and higher photoreactivity (usually up to ζ (photonic efficiency) = 10%) [4–9]. However, more often than not, two main limitations hamper the photocatalytic activities of TiO_2 including wide bandgap ($\approx 3.2\, eV$ for anatase TiO_2) and fast recombination of the photogenerated electron-hole pairs. The bandgap of TiO_2 can only be motivated by ultraviolet (UV) light that restricts its utilization in visible light zone of the solar spectrum [10,11]. For achieving solar water splitting reaction, it is essential to develop visible-light responsive photocatalysts. Many metal sulfides can respond to visible light range because of the relatively higher valence band (VB) position than those of corresponding metal oxides, and more negative conductor conduction band (CB) position which is suitable for H_2O reduction [12–14]. Ternary sulfide $ZnIn_2S_4$ is one of the most attractive photocatalytic materials for the conversion of

solar energy into hydrogen energy due to the narrow band gap (2.4 eV) [15–18]. Nevertheless, it is difficult to use $ZnIn_2S_4$ as a single photocatalyst for splitting water into H_2 and O_2 because the photogenerated holes can oxidize the $ZnIn_2S_4$ itself rather than water, which resulting in no O_2 evolution and photocorrosion [19,20]. Therefore, construction of heterostructure photocatalysts system seems to be a feasible strategy that can respond to visible light and improve the photoexcited electron-hole separation, and it is important in the field of photocatalysis [21–23].

The artificial Z-scheme that mimic the natural photosynthesis is generally composed of two different photocatalysts and a suitable electron media [24,25]. The remarkable advantages of the Z-scheme systems include better separation efficiency of the photogenerated electron-hole pairs and stronger reduction/oxidation potentials on different active sites [26]. The reduction evolving photocatalyst as H_2 evolution system offers the reduction sites by CB electrons, and the oxidation evolving photocatalyst as O_2 evolution system provides the oxidation sites by VB holes. Reversible mediator (e.g., Fe^{3+}/Fe^{2+}, and IO_3^-/I^-) are applied to electron transport chain in Z-scheme systems for a long time [27,28]. Nevertheless, the ionic redox couples may result in relaying electrons in solution, and the all-solid-state Z-scheme system is more favorable by using of solid electron mediator [29].

Noble metals (such as Au and Ag) and reduced graphene oxide (RGO) have often been used as electron mediators [30–32]. The electron mediators provide a pathway through which the photogenerated electrons in one semiconductor can travel and recombine with the holes in another semiconductor quickly, leaving more reductive electrons and more oxidative holes to participate in the redox reactions in the corresponding active sites. Tada and his coworkers first reported TiO_2-Au-CdS all-solid-state Z-scheme systems that pioneer the gold nanoparticles (Au NPs) as electron transfer mediator [33]. More recently, environmentally friendly ternary Z-scheme heterojunction was studied, and the results also demonstrated Au NPs could act as contact interface between electron accepting and donating photocatalyst [34–37]. Therefore, it is expected that Au NPs can be used to construct Z-scheme systems that consisting of metal sulfide photocatalysts with high H_2 evolution ability for water splitting.

Herein, we prepared an elegant all-solid-state urchin-like $ZnIn_2S_4$-Au-TiO_2 Z-scheme composite for improving photocatalytic water splitting activity under solar light irradiation. It is worth pointing out that the metallic Au species act as the solid state electron mediator can enhance the transfer rate of the photogenerated electrons and holes between the photocatalysts. The designed $ZnIn_2S_4$-Au-TiO_2 materials have greatly overcome the weakness of single-component and came true high charge-separation efficiency and strong redox ability. Moreover, the Au NPs and $ZnIn_2S_4$ loadings are investigated and detailed mechanism toward the photocatalysis of this $ZnIn_2S_4$-Au-TiO_2 heterostructure has been further proposed.

2. Experimental

2.1. Synthesis of TiO_2 microsphere

Typically, 1.6 mL KCl solution (0.1 M) was added in 400 mL ethanol in round bottom flask with three necks (placed in a mixture of ice and water). 10 mL tetrabutyl titanate (TBOT) was added dropwise into above solution under vigorously magnetic stirring. The resulting white TiO_2 suspension was kept static at room temperature for 10 h, then the TiO_2 microsphere were collected by centrifugation, washed with ethanol and water for three times and kept at 60 °C for 10 h in an electric oven. Finally, the as-synthesized sample was sintered at 550 °C for 4 h (10 °C /min).

2.2. Synthesis of TiO_2 microsphere decorated with Au nanoparticles (Au-TiO_2)

160 mg of TiO_2 microsphere and 52 mg of Polyvinylpyrrolidone (PVP) was added to 80 mL of EG in a 250 mL round-bottom flask. The obtained suspension was transferred to and kept under vigorous stirring at 90 °C for 20 min. Then, 1 mL of a 120 mM $NaBH_4$ (aq) and 1 mL of a 24 mM $HAuCl_4$ (aq) solutions were sequentially added to the reaction flask. This mixture was kept under vigorous stirring for another1 h to produce Au-TiO_2, which were washed three times with ethanol and water by centrifugation.

2.3. Fabrication of $ZnIn_2S_4$-Au-TiO_2

The schematic of the preparation route of the ternary $ZnIn_2S_4$-Au-TiO_2 heterostructure is given in Scheme 1. In detail, a chemical-deposition process leads to the formation of Au NPs on the TiO_2 microsphere surface (namely Au-TiO_2). The TiO_2 microspheres possess large surface-exposure area, which enabled the uniform deposition of monodisperse Au NPs over the entire surface of the support. Then $ZnIn_2S_4$ nanosheet directly deposited on the surface of the Au-TiO_2 with a solvothermal process, and the ternary $ZnIn_2S_4$-Au-TiO_2 composite were formed. $ZnIn_2S_4$-Au-TiO_2 samples with different weight percentages of $ZnIn_2S_4$ and Au (denoted as x%-ZIS-y%Au-TO; x = 30, 40, 50, 60, and 70; y = 12, 24, 36 and 48) were prepared by the solvothermal

method. A certain amount of $ZnCl_2$, $InCl_3 \cdot 4H_2O$ and TAA were dissolved in 100 mL ethylene glycol and stirred at room temperature, to which an appropriate amount of as-prepared Au-TiO_2 was dispersed by sonication for another 0.5 h. The above mixture was maintained in the autoclave and heated to 120 °C for 2 h. At last, the products were washed with water and absolute ethanol and dried at 70 °C. For comparation, Au-$ZnIn_2S_4$-TiO_2 composite was also prepared by desposition Au NPs on $ZnIn_2S_4$-TiO_2 in the same condition.

2.4. Characterizations

The crystallinity of the as-synthesized samples were measured by X-ray diffraction (XRD) on a Bruker D8A A25X X-ray diffractometer system using Cu Kα (λ = 0.15406 nm) radiation. The morphologies and structure of the prepared samples were tested by using a HITACHI S-4800 field emission scanning electron microscope (SEM) instrument at 10KV and 5 μA. High-resolution transmission electron microscopy (HR-TEM) and energy-dispersive X-ray spectroscopy (EDS) were applied to investigate the microstructure using a JEOL JEM-2010 instrument (HR-TEM operated at 200 kV). The UV–vis diffuse reflectance spectra (DRS) of the samples were tested on a TU-1901 double beam spectrophotometer and $BaSO_4$ was used as the reference. The photoluminescence (PL) spectra were measured at 25 °C under excitation by incident light of 375 nm using a Hitachi F-4600 fluorescence spectrometer. X-ray photoelectron spectroscopy (XPS) of the as-prepared samples was performed on a K-Alpha spectrometer (THERMO FISHER SCIENTIFIC). Nitrogen adsorption-desorption isotherms were determined by a Quadrasorb SI-MP. The specific surface area of the sample was calculated by the BETmethod.

2.5. Measurement of photocatalytic Water splitting

Photocatalytic water splitting was investigated under simulated solar light. A 300 W Xe lamp was used as light source with the electric current at 15 A. In a typical process for testing the photocatalytic hydrogen evolution, 0.05 g photocatalyst was dispersed in 100 mL water in a quartz reactor. The mixture was dispersed by ultrasonic stirring for 15 min, and then was irradiated under UV–vis light with magnetic stirring. The gas products from photocatalytic reactions were periodically monitored and analyzed using gas chromatography (GC-2014, Shimadzu Corp, Japan).

3. Results and discussion

The X-Ray Diffraction (XRD) pattern (Fig. 1 S1, Supporting Information) indicates that the precursor samples are amorphous and transform into anatase phase after calcination treatment. Fig. 1a shows the XRD data of as-prepared samples at various stages. The dominant peaks can be indexed to the anatase TiO_2 pattern (JCPDS, No 21–1272), while the diffraction peaks of the Au (200) at 44.4° and Au (111) at 77.8° are obviously detected over Au-TiO_2. A typical XRD pattern of the $ZnIn_2S_4$-Au-TiO_2 products can be clearly identified the existence of TiO_2, Au and $ZnIn_2S_4$ in the composite structures. Moreover, no other impurity-related diffraction peaks are detected, indicating the sample has high purity. The UV–vis spectra of TiO_2, Au-TiO_2 and $ZnIn_2S_4$-Au-TiO_2 composite are shown in Fig. 1b. The absorption edge of pristine TiO_2 microspheres is around 415 nm, which is larger than the TiO_2 nanoparticle (387 nm). This phenonmenon comes from the quantum effect of the larger size of TiO_2 microspheres. With the introduction of Au NPs, the Au-TiO_2 shows strong absorption in the visible region which could be attributed to the surface plasmon resonance (SPR) of Au NPs. The pure $ZnIn_2S_4$ nanosheets exhibit apparent visible absorption region. In comparison to the Au-TiO_2, the absorption peak of the $ZnIn_2S_4$-Au-TiO_2 is obviously red-shifted due to the photosensitizing effect of the incorporated $ZnIn_2S_4$ nanosheets. Furthermore, the absorption intensity is also found to gradually increase, which exhibit the
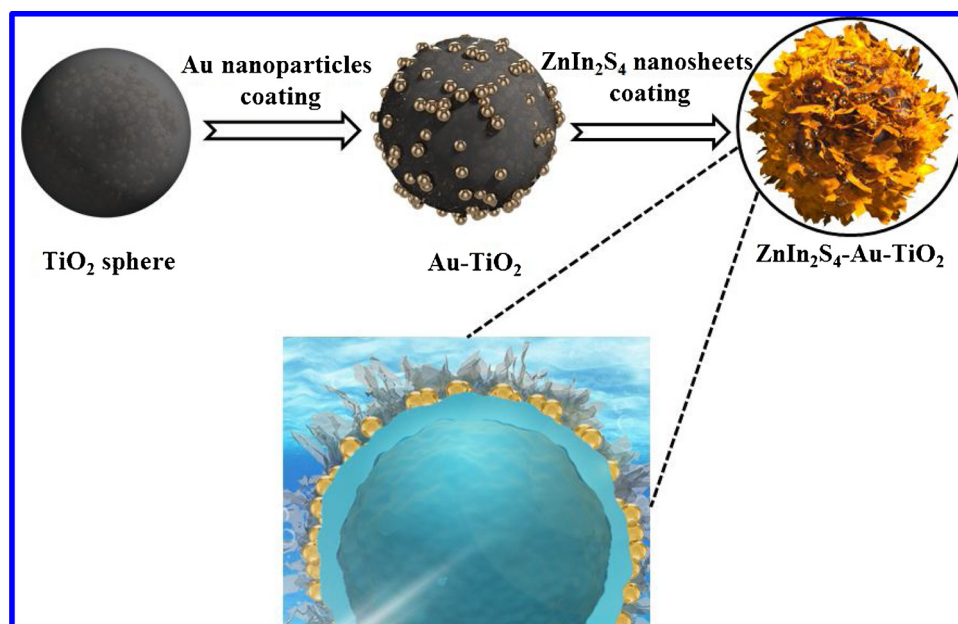
Scheme 1. Schematic illustration of the fabrication process of $ZnIn_2S_4$-Au-TiO_2 photocatalyst: Au-TiO_2 is prepared by a chemical-deposition process and $ZnIn_2S_4$-Au-TiO_2 is synthisized by solvothermal process.

promoted charge-carrier separation rising from the SPR-coupling effect and enhanced utilization of solar light [38,39].

It can be seen from Fig. 2a that the TiO_2 samples are well-defined solid spheres with sizes of 400∼500 nm. As shown in Fig. S2 (Supporting information), there is no obvious morphology change between amorphous sample and crystal phase. After Au NPs loaded on TiO_2, the surface of the TiO_2 spheres becomes obviously rough (Fig. 2b). Besides, Au NPs adsorbed onto the TiO_2 surface could be confirmed by the color change of the original TiO_2 suspension from white to purple after the reaction. The urchin-like $ZnIn_2S_4$-Au-TiO_2 microstructure is obtained by $ZnIn_2S_4$ nanosheets self-organized onto the surface of Au-TiO_2 composite colloidal microspheres through solvothermal method (Fig. 2c). A more detailed structural analysis can be seen in Fig. 2d, the present $ZnIn_2S_4$-Au-TiO_2 microspheres with a diameter of ∼1 μm are comprised of large interleaving flakes.

The morphology of the as-prepared samples further characterized by TEM. Fig. 3a and b show the low and high magnification TEM images of the TiO_2 microspheres. The TiO_2 microspheres have a relatively uniform diameter of about 500 nm, which is composed of small anatase TiO_2 nanoparticle with sizes of about 5–10 nm [40,41]. The TEM images of Au-TiO_2 show that highly uniform Au NPs with an average diameter of 20 nm evenly distributed on the surface of TiO_2 microspheres (Fig. 3c), indicating that the successful deposition of Au NPs (Fig. S3a, Supporting information). As seen from Fig. 3d, the Au NPs are firmly deposited on the anatase TiO_2 surface with an orientation relationship of Au [111]//TiO_2 [101], which can be verified by the lattice spaces of 0.30 and 0.36 nm. The corresponding selected area electron diffraction (SAED) pattern also displayed two kinds of characteristic spots, further confirming the formation of Au NPs coating (Fig. S3d, Supporting information). The TEM and HRTEM images show that large number of $ZnIn_2S_4$ nanosheets have grown on the surface of TiO_2 microspheres to forming urchin-like $ZnIn_2S_4$-Au-TiO_2 nanojunction, possibly due to the strong interaction between $ZnIn_2S_4$ and TiO_2 (Fig. 3e and f) [42]. The corresponding Energy dispersive X-ray (EDS) spectrum of the composite is shown in Fig. S4 (Supporting information), which revealed that the composite included five elements, Ti, O, Au, Zn, In and S. The ultrathin $ZnIn_2S_4$ nanosheets not only improve the light absorption of visible light, but also enhance the transfer rate of the
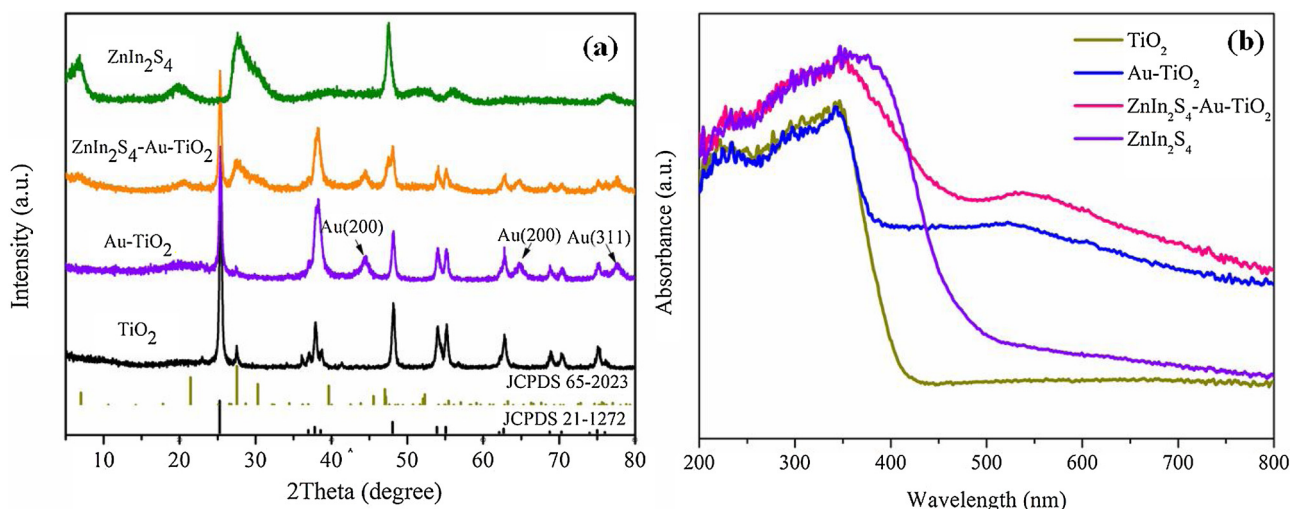
Fig. 1. (a) Crystalline structure and (b) UV–vis diffuse reflectance spectra of TiO_2, Au-TiO_2, $ZnIn_2S_4$-Au-TiO_2 and $ZnIn_2S_4$ samples.
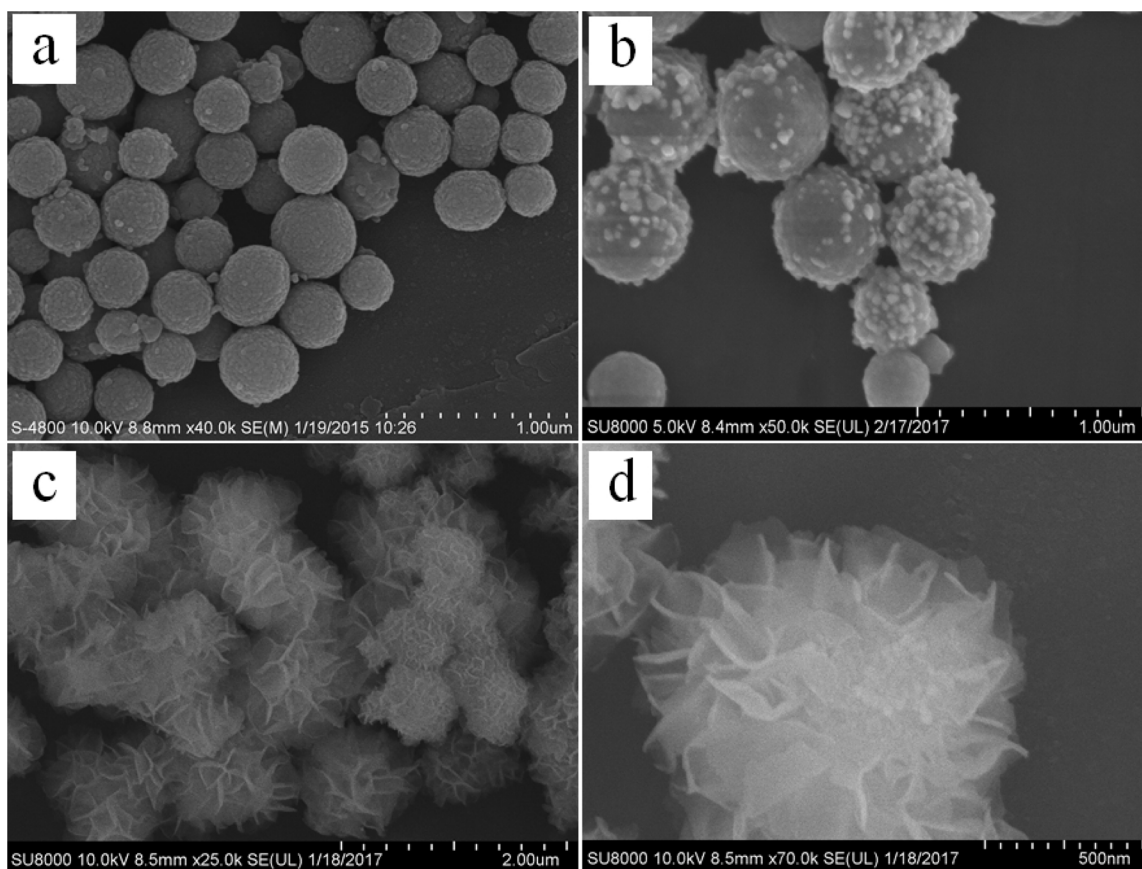
Fig. 2. SEM image of (a) TiO_2; (b) Au-TiO_2; (c) and (d) $ZnIn_2S_4$-Au-TiO_2 composite.

photogenerated charge carriers with minimum probability of recombination due to high carrier mobility [43]. The lattice structure of the $ZnIn_2S_4$ assembled on the Au NPs as shown in Fig. 3g. Compared with $ZnIn_2S_4$-TiO_2 photocatalyst and $ZnIn_2S_4$-Au-TiO_2 samples, the Au NPs with the uniformed sizes are well dispersed and assembled between the $ZnIn_2S_4$ nanosheets and TiO_2 microspheres (Fig. S5, Supporting information). The EDX elemental mapping of a single sphere (Fig. 3h) can be powerfully confirmed the expected sandwich structure. Besides, the TEM image of Au-$ZnIn_2S_4$-TiO_2 sample can be seen in Fig. S6 (Supporting information), and the selective distribution of Au NPs with a size of 5 nm onto the heterostructure of $ZnIn_2S_4$-TiO_2. These above-mentioned results indicate that the three-phase $ZnIn_2S_4$-Au-TiO_2 composite photocatalysts with the ideal heterostructure are successfully obtained.

The determination of surface area and porosity of the as-fabricated TiO_2, Au-TiO_2, $ZnIn_2S_4$ and $ZnIn_2S_4$-Au-TiO_2 samples are then tested to understand how these quantities plays roles in changing light absorption and photocatalytic performances. As shown in Fig. S7a (Supporting information), the samples of N_2 adsorption-desorption isothermal curve belong to II type curve, which demonstrates the pore structure formed by the aggregation of the particles. The pore size distribution by the Barrett-Joyner-Halenda (BJH) method is in the range of 2–20 nm (Fig. S7b). The feature of curve does not change after Au NPs loading which indicating the pore structure of TiO_2 is well maintained. However, there is a drastically decreases of the BET specific surface area (Table 1, Supporting Information), which may attributed to that Au NPs block the pore of the TiO_2 microsphere [44]. It should be noted that there is a significantly increased of BET specific surface area for $ZnIn_2S_4$-Au-TiO_2 ($63.53 \, m^2 \, g^{-1}$) compared with Au-TiO_2 microsphere ($5.53 \, m^2 \, g^{-1}$), suggesting that the nanosheet structure of $ZnIn_2S_4$ is favarable to increasing the specific surface area. A larger specific surface area may be conducive to enlarging the contact area between the catalysts and

reactants, so as to improve the photocatalytic performance.

The surface chemical compositions and states of the TiO_2, Au and $ZnIn_2S_4$ are investigated by X-ray photoelectron spectroscopy (XPS) in order to clarify the interactions of the as-fabricated photocatalyst. As shown in the survey scan XPS spectra (Fig. S8a), Ti2p and O1s peaks are observed for TiO_2 and Au-TiO_2, while S2p, In3d and Zn2p peaks are displayed for $ZnIn_2S_4$ and $ZnIn_2S_4$-Au-TiO_2 samples. Besides, the XPS peak of Au NPs is obvious at low resolution for Au-TiO_2. However, the peak of Au is indistinguishable for $ZnIn_2S_4$-Au-TiO_2 due to Au NPs is capped with $ZnIn_2S_4$. The high-resolution Ti2p, O1s, Au4f, Zn2p, In3d and S2p XPS spectra of $ZnIn_2S_4$-Au-TiO_2 are shown in Fig. 4, which confirms the presence of these elements in the typical composite sample. The binding energies of Ti 2p3/2 and Ti 2p1/2 for TiO_2 are located at 457.8 eV (main peak) and 463.7 eV with a splitting energy of 5.9 eV, presenting Ti^{4+} species in a tetragonal structure (Fig. 4a). The O1s located at about 529.2 eV corresponding to lattice oxygen of TiO_2 (Fig. 4b) [45]. The XPS signals of Ti and O are relatively weak may due to the over coating of $ZnIn_2S_4$, which makes it difficult to identify the exact nature of TiO_2. In Fig. 4c, the peak observed at a binding energy of 82.8 eV is ascribed to metallic Au 4f7/2, thus confirming that the Au species exist as metallic $Au°$ in $ZnIn_2S_4$-Au-TiO_2 [46,47]. The binding energies of Zn2p3/2 and Zn2p1/2 for $ZnIn_2S_4$ are located at 1021.70 eV and 1044.72 eV, which are consistent with the values for Zn^{2+} (Fig. 4d). In Fig. 4e, the characteristic peak at 445.03 eV (3d 5/2) and 452.61 eV (3d 3/2) are confirmed that the chemical state of In in the samples is $+3$. The S 2p 1/2 peak at 161.80 eV is ascribed to S coordinated to Zn and In in $ZnIn_2S_4$ (Fig. 4f). Once Au is introduced onto the TiO_2 core, the Ti 2p and O1s peak shifts to a higher binding energy of 458.2 eV (Fig. S8b and c). This shift is indicative of the interaction between Au and TiO_2 [48,49]. Such a similar phenomenon is also observed from the XPS spectra of S2p (Fig. S8d), In3d (Fig. S8e) and Z2p (Fig. S8f) peaks. That is, the binding energies of S2p (161.0 eV), In3d$_{5/2}$
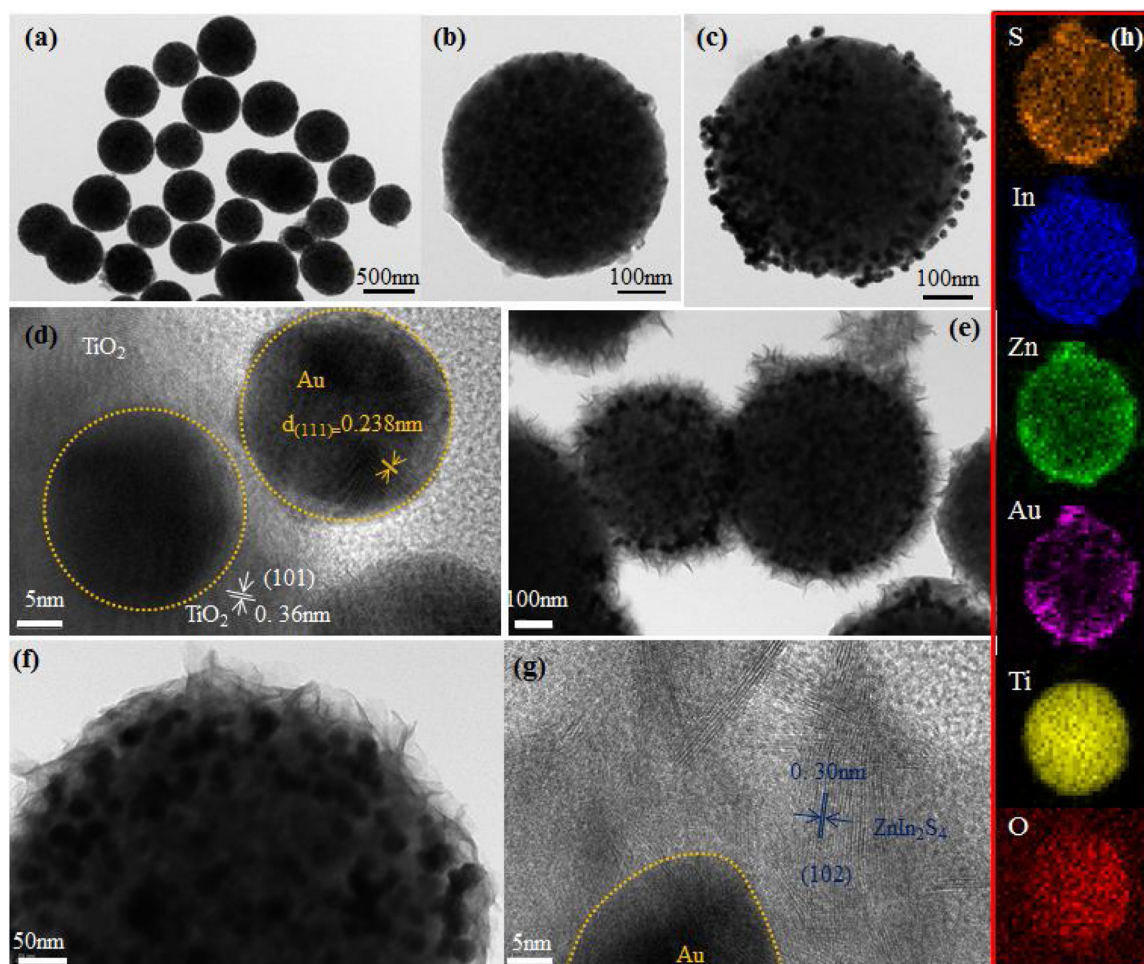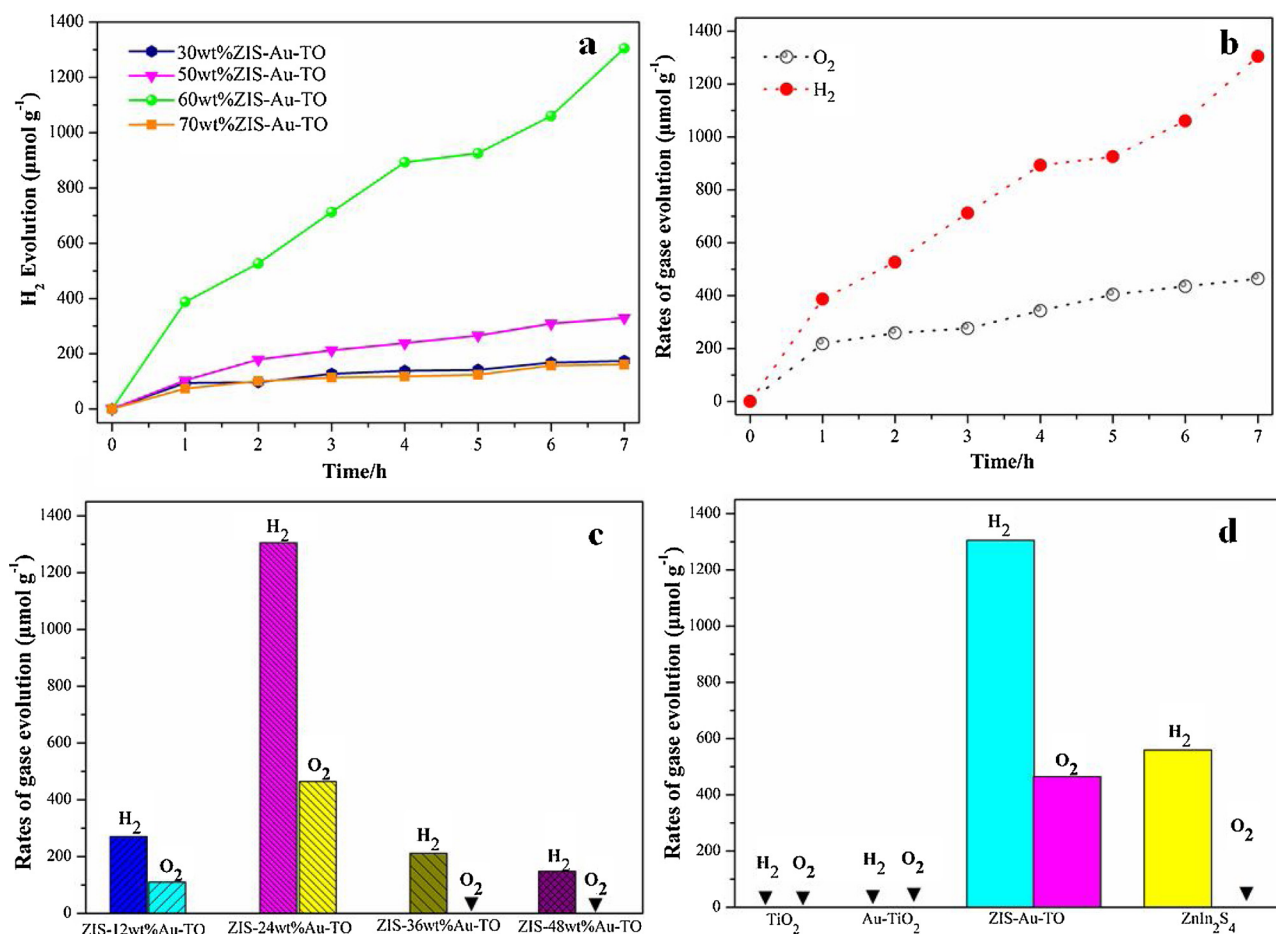
Fig. 3. (a–b) Typical TEM images of TiO$_2$ sphere; (c–d) TEM and HRTEM image taken at the interface between Au NPs and TiO$_2$; (e–h) TEM and HRTEM of ZnIn$_2$S$_4$-Au-TiO$_2$ composite and the corresponding EDS element-mapping data of Zn, In, S, Au, Ti, and O of a single sphere.
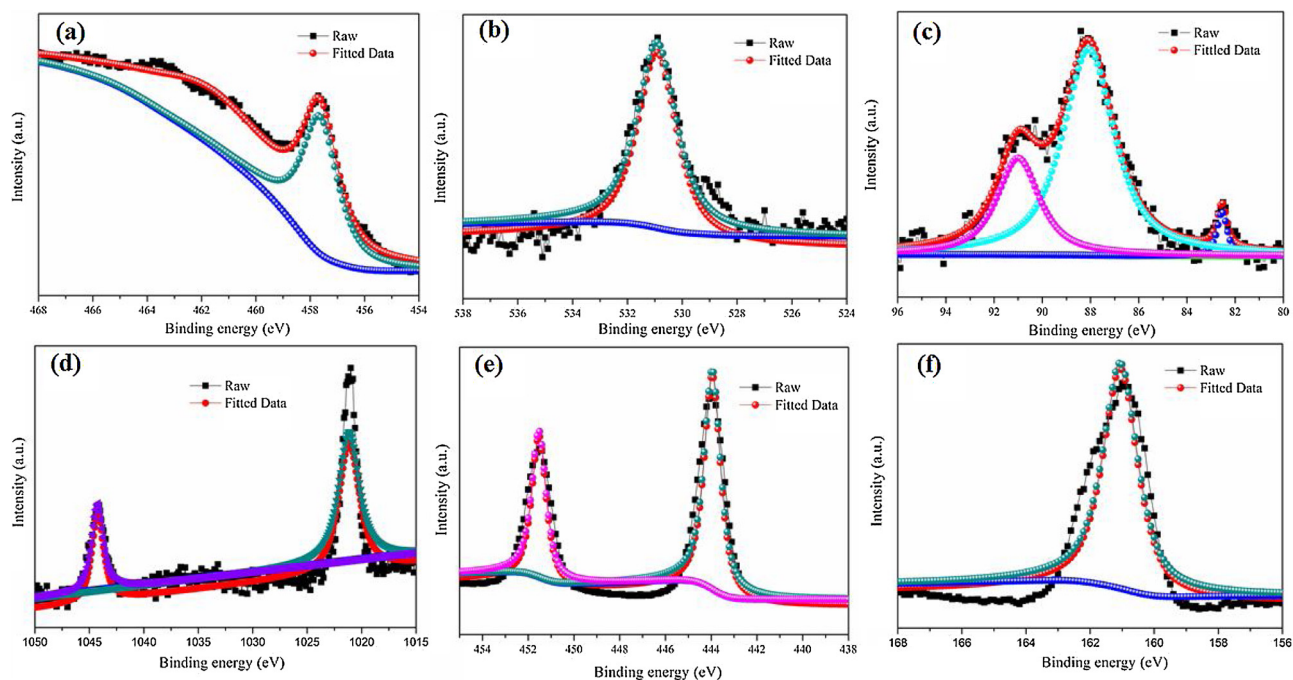
Fig. 4. XPS spectra for the as-obtained ZnIn$_2$S$_4$-Au-TiO$_2$ photocatalyst: (a) Ti2p; (b) O1s; (c) Au4f; (d) Zn2p; (e) In3d; (f) S2p.

Fig. 5. (a) Time courses of photocatalytic H_2 evolution from water of x%ZIS-24 wt%Au-TO with different $ZnIn_2S_4$ mass ratios; (b) H_2 and O_2 evolution of 60 wt%ZIS-24 wt%Au-TO sample via photocatalytic water-splitting; (c) photocatalytic H_2 and O_2 evolution from water of 60 wt%ZIS-y%Au-TO with different Au NPs mass ratios and (d) comparsion of photocatalytic activity for H_2 and O_2 production over various photocatalysts.

(444.1 eV), In3d$_{3/2}$ (451.5 eV), Z2p$_{3/2}$ (1021.2 eV) and Z2p$_{1/2}$ (1044.7 eV) of $ZnIn_2S_4$-Au-TiO$_2$ are lower than those of S2p (161.2 eV), In3d$_{5/2}$ (444.3 eV), In3d$_{3/2}$ (451.8 eV), Z2p$_{3/2}$ (1021.4 eV) and Z2p$_{1/2}$ (1044.9 eV) of pure $ZnIn_2S_4$. The XPS results implied the existence of chemical bonds in the $ZnIn_2S_4$-Au-TiO$_2$ [50].

The constructed ternary $ZnIn_2S_4$-Au-TiO$_2$ sample is used for photocatalytic water splitting under simulated sun light irradiation in the absence of sacrificial agent. Fig. 5a shows the effect of loading amount $ZnIn_2S_4$ on the efficiency of photocatalytic hydrogen evolution (the Au NPs is fixed (24 wt %)). It can be seen that the optimal loading amount of $ZnIn_2S_4$ is 60 wt%, which achieve the highest photocatalytic activity for H_2 production with the rate of 186.3 µmol g^{-1} h^{-1} (60 wt%ZIS-Au-TO). Further increasing the $ZnIn_2S_4$ loading amount led to a decreased H_2 evolution rate may due to the "light-shielding effect". [51] Thus, $ZnIn_2S_4$-Au-TiO$_2$ composite with 60 wt% $ZnIn_2S_4$ loading amount is chosen as the typical samples for further investigations. Meanwhile, the O_2 production rate of 60 wt%ZIS-Au-TO sample is detected in the photoreaction proceeding, and the result reached to 66.3 µmol g^{-1} h^{-1}. Notably, the amount of generated hydrogen is approximate twice that of oxygen production (H_2/O_2 = 2.8), indicating 2:1 stoichiometric water splitting (Fig. 5b). It should be mentioned that the content of Au NPs showed considerable influence on the photocatalytic activities in this ternary $ZnIn_2S_4$-Au-TiO$_2$ system. As observed in Fig. 5c, the H_2 and O_2 evolution are 270 µmol g^{-1} and 110 µmol g^{-1} with the Au NPs content at 12 wt%. With increasing of Au NPs content, the H_2 and O_2 evolution rate are enhanced and reach the maximum value (ZIS-24%Au-TO). There is a decrease photocatalytic activity with further increase loading amount of Au NPs. Interesting, no O_2 is detected may

due to that O_2 stops at the status of adsorbed $\cdot O_2^-$ (a form of Ti-O-O-Ti) [52], or Au NPs at higher coverages can compete for photogenerated holes at the interface of TiO$_2$ (TiO$_2$ (h) + Au$^\circ$ → TiO$_2$ + Au$^+$) [53]. Fig. 5d shows a comparison of H_2 production rates of TiO$_2$, Au-TiO$_2$, pure $ZnIn_2S_4$ and $ZnIn_2S_4$-Au-TiO$_2$ composite. Water splitting did not proceed using either TiO$_2$ or Au-TiO$_2$ catalysts attribute to the low energy level of their conduction bands, which are close to the standard potential of H^+/H_2. Pure $ZnIn_2S_4$ shows a very low photocatalytic activity with the H_2 evolution of 558 µmol g^{-1}, and with no O_2 evolution because of the photocorrosion. Importantly, there is an obvious increase of H_2 and O_2 production rate of $ZnIn_2S_4$-Au-TiO$_2$ compared with $ZnIn_2S_4$-TiO$_2$ and Au-TiO$_2$ photocatalysts (Fig. S9, Supporting information). The results indicating that combination of $ZnIn_2S_4$ with Au-TiO$_2$ was indispensable for water splitting. In order to show that the Au NPs act as an efficient electron transfer in $ZnIn_2S_4$-Au-TiO$_2$ system, the photocatalytic hydrogen activities of $ZnIn_2S_4$-Au-TiO$_2$ sample and Au NPS modified $ZnIn_2S_4$-TiO$_2$ heterostructure (Au-$ZnIn_2S_4$-TiO$_2$) is compared. The H_2 evolution rate of $ZnIn_2S_4$-Au-TiO$_2$ photocatalysts is almost 2 times of Au-$ZnIn_2S_4$-TiO$_2$ photocatalysts, suggesting that the surface loading of Au NPs might have little contribution to the improvement photoactivity activity (Fig. S10) [54]. These results confirmed the positive role of Au NPs in $ZnIn_2S_4$-Au-TiO$_2$ system for enhancing the photoactivity of TiO$_2$ and $ZnIn_2S_4$ catalysts under illumination. These results confirmed the Z-scheme model of ternary $ZnIn_2S_4$-Au-TiO$_2$ system.

To further understand the mechanism of enhanced of photocatalytic activity of $ZnIn_2S_4$-Au-TiO$_2$ system, transient photocurrent response and electrochemical impedance spectroscopy (EIS) are conducted under
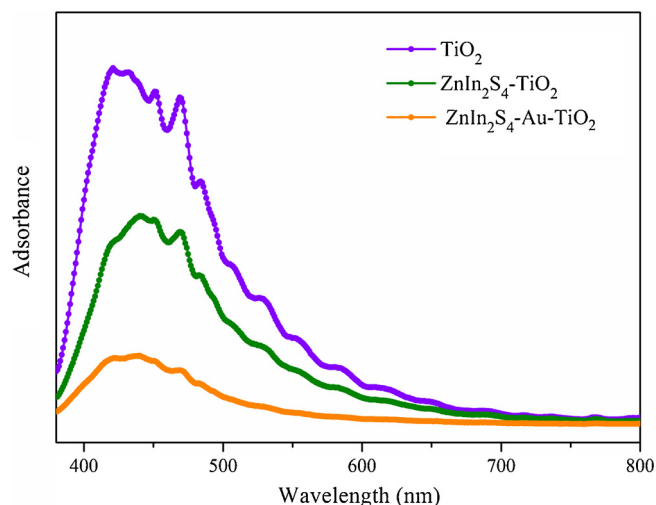
Fig. 6. Photoluminescence spectra of TiO$_2$, ZnIn$_2$S$_4$-TiO$_2$ and ZnIn$_2$S$_4$-Au-TiO$_2$ measured at room temperature with a 325 nm excitation wavelength.

UV–vis light irradiation. As presented in Fig. S11, the pulsed photocurrent density of the ZnIn$_2$S$_4$-Au-TiO$_2$ sample is higher than other photocatalysts, suggesting more efficient separation of photoexcited electron-hole pairs happened. In addition, the impedance radius of ZnIn$_2$S$_4$-Au-TiO$_2$ is smaller than ZnIn$_2$S$_4$-TiO$_2$ (Fig. S12), indicating that Au NPs can enhance separation efficiency of the photogenerated charges and facilitate the interfacial charge transfer. Futhermore, the strengthened interface charge carrier transfer and separation efficiency can be evidenced by photoluminescence (PL) emission spectroscopy. Fig. 6 shows the PL spectra of TiO$_2$, ZnIn$_2$S$_4$-TiO$_2$ and Au-ZnIn$_2$S$_4$-TiO$_2$ heterostructure. The emission peak of these three photocatalysts is observed at around of 450 nm. Although the ZnIn$_2$S$_4$-TiO$_2$ heterostructure shows similar PL emission bands to TiO$_2$, the band intensity is much weakened. While the ZnIn$_2$S$_4$-Au-TiO$_2$ composite shows lower intensity by comparing with both of TiO$_2$ and ZnIn$_2$S$_4$-TiO$_2$. It is

established that the charge-carrier transfer between different parts of composites usually results in the weakening of PL emission bands [55]. The effective Z-scheme charge-carrier transfer process mediated by the Au NPs at the interface of ZnIn$_2$S$_4$ and TiO$_2$ can well explain the quenching of PL emission in ZnIn$_2$S$_4$-Au-TiO$_2$, and thus improve its photocatalytic activity.

The photocatalytic mechanism is tentatively proposed for the water splitting over present designed Z-scheme ZnIn$_2$S$_4$-Au-TiO$_2$ heterostructure, as represented in Scheme 2. Under irradiation, both ZnIn$_2$S$_4$ and TiO$_2$ absorb light and generate photo-induced electron-hole pairs. The photo-induced holes are more likely remain in the VB of TiO$_2$, whereas electrons can be quickly transferred to the VB of ZnIn$_2$S$_4$ through deposited Au NPs. Therefore, the photoinduced electrons with strong reducibility are left on the CB of ZnIn$_2$S$_4$, and the photoinduced holes with strong oxidizability are accumulated on the VB of TiO$_2$. The holes stored in the VB of TiO$_2$ and enriched electrons in the CB of ZnIn$_2$S$_4$ are trapped by H$_2$O molecule near the surface to form O$_2$ and H$_2$. This enhanced photocatalytic activity occurs because Z-scheme heterostructure not only facilitates an effective spatial separation of photo-induced electron-hole pairs but also enhances the redox ability of photocatalyst caused by an increase in redox potential.

4. Conclusion

In conclusion, a ternary ZnIn$_2$S$_4$-Au-TiO$_2$ Z-scheme heterostructure photocatalyst has been successfully synthesized select Au NPs as a solid electron mediator. The deposit location of Au NPs shows great influence on the photocatalytic performance. The photocatalytic activity of obtained ZnIn$_2$S$_4$-Au-TiO$_2$ photocatalysts achieve the highest for H$_2$ production with the rate of 186.3 μmol g^{-1} h^{-1}, and the O$_2$ production rate is reached to 66.3 μmol g^{-1} h^{-1} for water splitting. The outstanding performance lies in the formation of effective vectorial Z-scheme charge-carrier transfer at the interface of the ZnIn$_2$S$_4$-Au-TiO$_2$, which could improve the separation efficiency of photoinduced carriers and remain the strong redox ability of the photocatalyst. It is expected that such finding will provide new insight into the design and
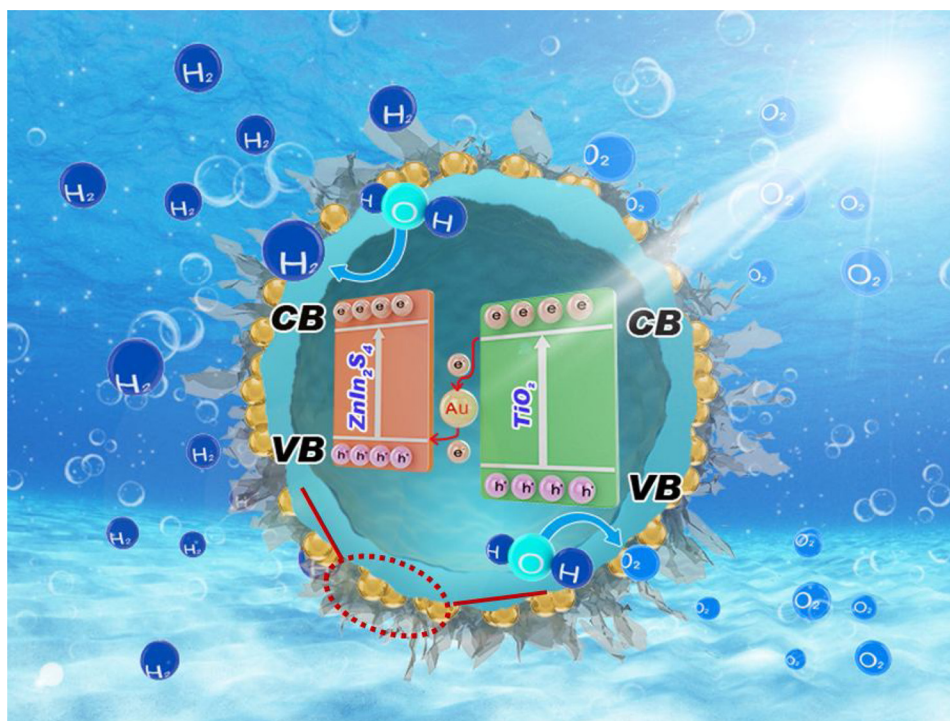
Scheme 2. Proposed schematic of Z-scheme charge-carrier transfer process in the ZnIn$_2$S$_4$-Au-TiO$_2$ Z-scheme photocatalysis system for water splitting under solar light irradiation.

underlying Z-scheme based functional materials.

Acknowledgements

This work is supported by the National Natural Science Foundations of China (Grant No.21577132), the Fundamental Research Funds for the Central Universities (Grant No. 2652015225)

Appendix A. Supplementary data

Supplementary material related to this article can be found, in the online version, at doi:https://doi.org/10.1016/j.apcatb.2018.04.038.

References

[1] A. Kudo, H. Kato, I. Tsuji, Chem. Lett. 33 (2004) 1534–1539.
[2] A. Kudo, Y. Miseki, Chem. Soc. Rev. 38 (2009) 253–278.
[3] X.B. Chen, S.H. Shen, L.J. Guo, S.S. Mao, Chem. Rev. 110 (2010) 6503–6570.
[4] M.G. Walter, E.L. Warren, J.R. McKone, S.W. Boettcher, Q.X. Mi, E.A. Santori, N.S. Lewis, Chem. Rev. 110 (2010) 6446–6473.
[5] X. Chen, S.S. Mao, Chem. Rev. 107 (2007) 2891–2951.
[6] M. Adachi, Y. Murata, J. Takao, J.T. Jiu, M. Sakamoto, F. Wang, J. Am. Chem. Soc. 126 (2004) 14943–14949.
[7] K. Maeda, K. Domen, J. Phys. Chem. Lett. 1 (2010) 2655–2661.
[8] M.D. Hernández-Alonso, F. Fresno, S. Suárez, J.M. Coronado, Energy Environ. Sci. 2 (2009) 1231–1257.
[9] G. Yang, H. Ding, D.M. Chen, W.H. Ao, J. Wang, X.F. Hou, Appl. Surf. Sci. 376 (2016) 227–235.
[10] J. Wang, D.N. Tafen, J.P. Lewis, Z.L. Hong, A. Manivannan, M.J. Zhi, M. Li, N.Q. Wu, J. Am. Chem. Soc. 131 (2009) 12290–12297.
[11] T. Butburee, Y. Bai, J. Pan, X. Zong, C. Sun, G. Liu, L. Wang, J. Mater. Chem. A 2 (2014) 12776–12784.
[12] K. Zhang, L.J. Guo, Catal. Sci. Technol. 3 (2013) 1672–1690.
[13] Y.Y. Zhang, Y.X. Tang, X.F. Liu, Z.L. Dong, H.H. Hng, Z. Chen, T.C. Sum, X.D. Chen, Small 9 (2013) 996–1002.
[14] H.G. Yu, X. Huang, P. Wang, J.G. Yu, J. Phys. Chem. C 120 (7) (2016) 3722–3730.
[15] G.P. Chen, N. Ding, F. Li, Y.Z. Fan, Y.H. Luo, D.M. Lia, Q.B. Meng, 2014, 160-161, 614–620.
[16] W. Chen, T.Y. Liu, T. Huang, X.H. Liu, X.J. Yang, Nanoscale 8 (2016) 3711–3719.
[17] L. Shang, C. Zhou, T. Bian, H.J. Yu, L.Z. Wu, C.H. Tung, T.R. Zhang, J. Mater. Chem. A 1 (2013) 4552–4558.
[18] Z.B. Lei, W.S. You, M.Y. Liu, G.H. Zhou, T. Takata, M. Hara, K. Domen, C. Li, Chem. Commun. (2003) 2142–2143 0.
[19] K. Iwashina, A. Iwase, Y.H. Ng, R. Amal, A. Kudo, J. Am. Chem. Soc. 137 (2015) 604–607.
[20] L. Wei, Y.J. Chen, Y.P. Lin, H.S. Wu, R.S. Yuan, Z.H. Li, Appl. Catal. B 144 (2014) 521–527.
[21] M. Ge, Y.F. Li, L. Liu, Z. Zhou, W. Chen, J. Phys. Chem. C 115 (2011) 5220–5225.
[22] Y. Hou, F. Zuo, A. Dagg, P.Y. Feng, Nano Lett. 12 (2012) 6464–6473.
[23] Y.J. Wang, Q.S. Wang, X.Y. Zhan, F.M. Wang, M. Safdar, J. He, Nanoscale 5 (2013) 8326–8339.
[24] G.A. Ozin, Energy Environ. Sci. 8 (2015) 1682–1684.
[25] H.J. Li, Y.Y. Gao, Y. Zhou, F.T. Fan, Q.T. Han, Q.F. Xu, X.Y. Wang, M. Xiao, C. Li, Z.G. Zou, Nano Lett. 16 (2016) 5547–5552.
[26] X.W. Wang, L.C. Yin, G. Liu, Chem. Commun. 50 (2014) 3460–3463.
[27] H. Kato, Y. Sasaki, N. Shirakura, A. Kudo, J. Mater. Chem. A 1 (2013) 12327–12333.
[28] P.J. Yang, J.H. Zhao, J. Wang, B.Y. Cao, L. Li, Z.P. Zhu, J. Mater. Chem. A 3 (2015) 8256–8259.
[29] A. Iwase, Y.H. Ng, Y. Ishiguro, A. Kudo, R. Amal, J. Am. Chem. Soc. 133 (2011) 11054–11057.
[30] H.J. Li, Y.Y. Gao, Y. Zhou, F.T. Fan, Q.T. Han, Q.F. Xu, X.Y. Wang, M. Xiao, C. Li, Z.G. Zou, Nano Lett. 16 (2016) 5547.
[31] A. Iwase, Y.H. Ng, Y. Ishiguro, A. Kudo, R. Amal, J. Am. Chem. Soc. 133 (2011) 11054.
[32] P. Wang, Y. Sheng, F.Z. Wang, H.G. Yu, Appl. Catal. B Environ. 220 (2018) 561–569.
[33] H. Tada, T. Mitsui, T. Kiyonaga, T. Akita, K. Tanaka, Nat. Mater. 5 (2006) 782–786.
[34] J. Li, S.K. Cushing, P. Zheng, T. Senty, F. Meng, A.D. Bristow, A. Manivannan, N. Wu, J. Am. Chem. Soc. 136 (2014) 8438–8449.
[35] Z.B. Yu, Y.P. Xie, G. Liu, G.Q. Lu, X.L. Ma, H.M. Cheng, J. Mater. Chem. A 1 (2013) 2773–2776.
[36] J.Q. Li, H. Yuan, Z.F. Zhu, J. Mol. Catal. A Chem. 410 (2015) 133–139.
[37] H.J. Li, Y.Y. Gao, Y. Zhou, F.T. Fan, Q.T. Han, Q.F. Xu, X.Y. Wang, M. Xiao, C. Li, Z.G. Zou, Nano Lett. 16 (2016) 5547–5552.
[38] L.Q. Liu, T.D. Dao, R. Kodiyath, Q. Kang, H. Abe, T. Nagao, J.H. Ye, Adv. Funct. Mater. 48 (2014) 7754–7762.
[39] L.W. Zhang, H.B. Fu, Y.F. Zhu, Adv. Funct. Mater. 18 (2008) 2180–2189.
[40] M. Ye, Q. Zhang, Y. Hu, J. Ge, Z. Lu, L. He, Z. Chen, Y. Yin, Chem. Eur. J. 16 (2010) 6243–6250.
[41] S.Y. Chae, M.K. Park, S.K. Lee, T.Y. Kim, S.K. Kim, W.I. Lee, Chem. Mater. 15 (2003) 3326.
[42] G. Yang, D.M. Chen, H. Ding, J.J. Feng, J.Z. Zhang, Y.F. Zhu, S. Hamid, D.W. Bahnemann, Appl. Catal. B Environ. 219 (2017) 611–618.
[43] H.J. Li, Y.Y. Gao, Y. Zhou, F.T. Fan, Q.T. Han, Q.F. Xu, X.Y. Wang, M. Xiao, C. Li, Z.G. Zou, Nano Lett. 16 (2016) 5547–5552.
[44] Y.J. Li, L.M. Yu, N. Li, W.F. Yan, X.T. Li, J. Colloid Interface Sci. 450 (2015) 246–253.
[45] H. Zhao, M. Wu, J. Liu, Z. Deng, Y. Li, B.L. Su, Appl. Catal. B Environ. 184 (2016) 182–190.
[46] K.M. Eblagon, M.F.R. Pereira, J.L. Figueiredo, Appl. Catal. B Environ. 184 (2016) 381–396.
[47] J.Q. Li, H. Yuan, Z.F. Zhu, J. Mol. Catal. A Chem. 410 (2015) 133–139.
[48] J. Wang, D.N. Tafen, J.P. Lewis, Z.L. Hong, A. Manivannan, M.J. Zhi, M. Li, N.Q. Wu, J. Am. Chem. Soc. 131 (2009) 12290–12297.
[49] Q. Zhang, D.Q. Lima, I. Lee, F. Zaera, M.F. Chi, Y.D. Yin, Angew. Chem. 123 (2011) 7226–7230.
[50] H.F. Shi, G.Q. Chen, C.L. Zhang, Z.G. Zou, ACS Catal. 4 (2014) 3637–3643.
[51] Z.Y. Zhang, Y.Z. Huang, K.C. Liu, L.J. Guo, Q. Yuan, B. Dong, Adv. Mater. 27 (2015) 5906–5914.
[52] V. Subramanian, E.E. Wolf, P.V. Kamat, Langmuir 19 (2003) 469–474.
[53] D.W. Li, S.X. Ouyang, H. Xu, D. Lu, M. Zhao, X.L. Zhang, J.H. Ye, Chem. Commun. 52 (2016) 5989–5992.
[54] J.W. Chiou, S.C. Ray, H.M. Tsai, C.W. Pao, F.Z. Chien, W.F. Pong, C.H. Tseng, J.J. Wu, M.H. Tsai, C.H. Chen, H.J. Lin, J.F. Lee, J.H. Guo, J. Phys. Chem. C 115 (2011) 2650–2655.
[55] Y. Hu, H.H. Qian, Y. Liu, G.H. Du, F.M. Zhang, L.B. Wang, X. Hu, CrystEngComm 13 (2011) 3438–3443.